



Validation of a CFD model with a synchronized triple-lidar system in the wind turbine induction zone

Meyer Forsting, Alexander Raul; Troldborg, Niels; Murcia Leon, Juan Pablo; Sathe, Ameya; Angelou, Nikolas; Vignaroli, Andrea

Published in:
Wind Energy

Link to article, DOI:
[10.1002/we.2103](https://doi.org/10.1002/we.2103)

Publication date:
2017

Document Version
Publisher's PDF, also known as Version of record

[Link back to DTU Orbit](#)

Citation (APA):
Meyer Forsting, A. R., Troldborg, N., Murcia Leon, J. P., Sathe, A., Angelou, N., & Vignaroli, A. (2017). Validation of a CFD model with a synchronized triple-lidar system in the wind turbine induction zone. *Wind Energy*, 20, 1481-1498. <https://doi.org/10.1002/we.2103>

General rights

Copyright and moral rights for the publications made accessible in the public portal are retained by the authors and/or other copyright owners and it is a condition of accessing publications that users recognise and abide by the legal requirements associated with these rights.

- Users may download and print one copy of any publication from the public portal for the purpose of private study or research.
- You may not further distribute the material or use it for any profit-making activity or commercial gain
- You may freely distribute the URL identifying the publication in the public portal

If you believe that this document breaches copyright please contact us providing details, and we will remove access to the work immediately and investigate your claim.

RESEARCH ARTICLE

Validation of a CFD model with a synchronized triple-lidar system in the wind turbine induction zoneA. R. Meyer Forsting¹, N. Troldborg, J. P. Murcia Leon, A. Sathe¹, N. Angelou and A. Vignaroli

Department of Wind Energy, Technical University of Denmark, Frederiksborgvej 399, 4000, Roskilde, Denmark

ABSTRACT

A novel validation methodology allows verifying a CFD model over the entire wind turbine induction zone using measurements from three synchronized lidars. The validation procedure relies on spatially discretizing the probability density function of the measured free-stream wind speed. The resulting distributions are reproduced numerically by weighting steady-state Reynolds averaged Navier-Stokes simulations accordingly. The only input varying between these computations is the velocity at the inlet boundary. The rotor is modelled using an actuator disc. So as to compare lidar and simulations, the spatial and temporal uncertainty of the measurements is quantified and propagated through the data processing. For all velocity components the maximal difference between measurements and model are below 4.5% relative to the average wind speed for most of the validation space. This applies to both mean and standard deviation. One rotor radius upstream the difference reaches maximally 1.3% for the axial component. Copyright © 2017 John Wiley & Sons, Ltd.

KEYWORDS

validation; lidar; CFD; blockage effect; upstream flow; induction zone; uncertainty quantification

CorrespondenceA. R. Meyer Forsting, Department of Wind Energy, Technical University of Denmark, Frederiksborgvej 399, 4000 Roskilde, Denmark.
E-mail: alrf@dtu.dk

Received 21 December 2015; Revised 8 February 2017; Accepted 13 February 2017

NOMENCLATURE

\mathbf{V}	velocity vector $\mathbf{V} = \{u, v, w\}$
\mathbf{x}	position vector $\mathbf{x} = \{x, y, z\}$
$\mathcal{N}(\mu, \sigma)$	normal distribution with mean μ and standard deviation σ
$V_{\infty}^{\min}, V_{\infty}^{\max}$	boundaries of validation space
$f(\bullet; \bullet)$	probability density function (pdf), semi-colon separates sample-space and function variables
i	triple-lidar data point index
j	triple-lidar cell index
k	index of wind speed bin
p	participation factor (equation (18))
θ	misalignment angle between rotor and triple-lidar reference frame
σ_{ϕ}	standard deviation of a quantity ϕ
$\bar{\phi}$	mean of a quantity ϕ
n_{ϕ}	total number of points discretizing ϕ
\bullet_{CFD}	quantity derived from CFD simulations
\bullet_{3l}	quantity derived from triple-lidar measurements
\bullet_{∞}	free-stream reference
\bullet'	triple-lidar coordinate system

1. INTRODUCTION

Power generating wind turbines exert a thrust force on the incoming flow, inducing a deceleration in the upstream region close to the rotor. The area in which this effect is noticeable is commonly referred to as the induction zone. The IEC standards for power performance measurements¹ assume this region to have a negligible effect beyond four radii (R) upstream, such that velocity measurements at hub height beyond this distance should give a reliable indication of the free-stream velocity on which to base a turbine's power curve. This free-stream velocity is an artificial construct as it is defined as the velocity that would have been measured at the rotor centre if there was no turbine. Measuring the power curve reference velocity at least $4R$ away from the turbine to avoid the induction zone, might however violate the very definition of the free-stream. Especially when considering the large rotor dimensions reached nowadays ($R > 80$ m), the flow evolution over this distance and the resulting time lag might decorrelate the measured wind field and the one interacting with the wind turbine. This is also the case for turbines in complex surroundings, which include mountainous terrain, forest or wind farms. Measuring closer to the turbine and thus inside the induction zone would partly offset the uncertainty from flow evolution. Replacing met masts with nacelle-mounted lidars would allow such measurements without disturbing the flow approaching the turbine. Wagner *et al.*² established that this is a viable approach to power curve validation. Nacelle lidars are furthermore tracking the wind direction, potentially decreasing the time for acquiring a full power curve, as more wind sectors become available. Likewise, it can become an input to preview-based control strategies, enabling the turbine to dynamically adapt to the incoming wind field, as suggested by Schlipf *et al.*³ Nevertheless, measuring inside the induction zone and predicting the wind field evolution requires a robust model capturing the flow upstream of a turbine accurately. Medici *et al.*⁴ compared a linear vortex model with wind tunnel measurements and a computational fluid dynamics (CFD) simulation. They extracted the flow-field of three small-scale wind turbine models from laser particle image velocimetry and hot wire measurements. The final inter-comparison along the turbines axis of symmetry showed matching trends. Howard and Guala⁵ similarly compared wind tunnel experiments and the simple vortex sheet model but furthermore included lidar field measurements. This work was spatially extended by Simley *et al.*,⁶ measuring with a synchronized triple-lidar system over half a turbine rotor. Similar to the work of Medici *et al.*,⁴ these studies showed agreeing trends, but the model's validity was not proven. Simley's work involving the triple-lidar system formed the basis for a measurement campaign in the inflow region of a 500 kW wind turbine in the summer of 2014 as part of the UniTTe project (www.unitte.dk). This lidar system captured all three velocity components over a large area, providing a unique dataset for model validation. In this paper, a probabilistic methodology for validating a high-fidelity CFD model with this dataset is presented. The inherently variable nature of the wind requires special treatment, such that the boundary conditions of the field experiment can be matched in the numerical simulations.

Failing to incorporate the variability of the wind speed ultimately leads to similarly inconclusive results regarding model validity as those of Medici⁴ and Howard⁵ as shown in Figure 1.

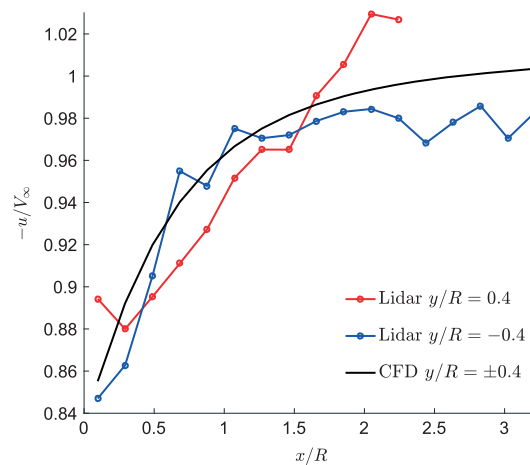


Figure 1. Axial velocity evolution upstream of wind turbine along two lines perpendicular to the rotor. The turbine is located at $x/R = 0$. The lidar data were averaged over a 30 min period with a free-stream velocity of 10.3 m/s. This velocity was set as inlet condition to the steady-state CFD (RANS-AD) simulation. [Colour figure can be viewed at wileyonlinelibrary.com]

These results underwent exactly the same post-processing as the data presented in Section 6 of this paper, excluding the probabilistic validation procedure. Instead, the lidar data were averaged over a 30 min period and compared with a CFD simulation at the free-stream velocity of 10.3 m/s. Again, the results in Figure 1 follow the same trend: as the flow approaches the turbine ($x \rightarrow 0$), the axial velocity component (u) diminishes, owing to the turbine-induced blockage. However, whereas the line $y/R = -0.4$ appears to match the numerical simulations, the other line shows strong disagreement with regards to the nature of this deceleration. This figure only serves as an example of a phenomenon registered across all measurements and is not limited to temporal averages. Any kind of sorting and averaging introduces some bias into model validation, by making the validation space a function of the sorting process. This encourages tuning the sorting parameters and limiting the validation space, which jeopardizes proper model validation. Note that the development of a validation procedure that utilizes data to its full extent also became a necessity owing to the scarcity of measurements. Apart from the validation method, several post-processing levels of the triple-lidar data are needed that propagate the measurement uncertainty. The complexity of the numerical simulations was reduced by employing a steady-state Reynolds Averaged Navier-Stokes (RANS) model and representing the rotor by an actuator disc. Validating this high-fidelity model is expected to allow the development of less computationally expensive methods.

2. VALIDATION METHODOLOGY

The validation approach relies on incorporating the inherently variable nature of field measurements into the numerical model. This is achieved by treating the boundary conditions of the experiment stochastically, in particular the estimated free-stream velocity, as it essentially determines the thrust exerted by the turbine. The free-stream velocity is a theoretical quantity that describes the velocity at the rotor centre as if there was no turbine. Therefore, it is only a function of time $V_\infty(t)$. Assuming that the rotor thrust, and with it the induction zone, is fully determined by the instantaneous free-stream velocity, the velocity field upstream can be expressed as a function of free-stream velocity, space and time $\mathbf{V}(V_\infty, \mathbf{x}, t)$. A measurement instrument with infinite spatial and temporal resolution would sample exactly this velocity. Assuming that this device periodically revisits the same probe locations after a time Δt_s , the following relationship can be established: $(x(t_0 + l\Delta t_s), y(t_0 + l\Delta t_s)) = (x_0, y_0)$, where l denotes the period number. This point will have seen free-stream velocities of $V_\infty(t_0 + l\Delta t_s)$. If the device's probe location moves in time, then with $\Delta t < \Delta t_s$, a new measurement location is obtained $(x(t_0 + \Delta t + l\Delta t_s), y(t_0 + \Delta t + l\Delta t_s)) = (x_{\Delta t}, y_{\Delta t})$. Equally, the free-stream velocity would be sampled with a time shift $V_\infty(t_0 + \Delta t + l\Delta t_s)$. Therefore each measurement point in \mathbf{x} has its own free-stream time series that depends on the number of periods l as shown in Figure 2. Finally, grouping all measurements for each point in space over time, the free-stream velocity and the measured velocities can be expressed with probability density functions $f(V_\infty; \mathbf{x})$ and $f(\mathbf{V}; \mathbf{x})$. Note that f is a function of \mathbf{x} , but a density over the sample-space variables to the left of the semi-colon. This notation is used throughout the paper.

Two free-stream pdfs and their approximation by a histogram with n_{V_∞} number of free-stream velocity bins are shown schematically in Figure 3. Each bin represents one CFD simulation with a deterministic boundary condition given by V_∞ . By weighting the CFD solutions $\mathbf{V}_{\text{CFD}}(V_\infty, \mathbf{x})$ according to $f(V_\infty; \mathbf{x})$, $f(\mathbf{V}; \mathbf{x})$ can be reconstructed numerically. Mean and

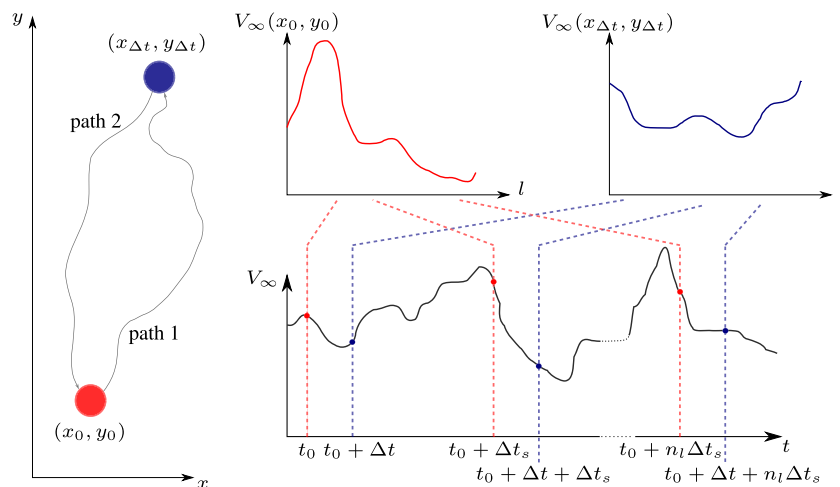


Figure 2. Sampling of the free-stream velocity V_∞ at two different points in time and space. [Colour figure can be viewed at wileyonlinelibrary.com]

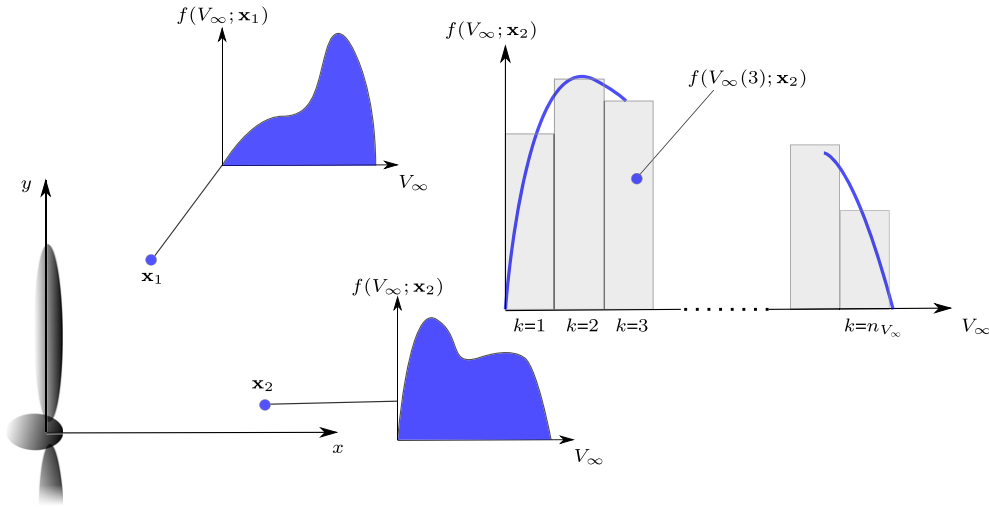


Figure 3. Probability density functions of the free-stream velocity at two measurement locations in the induction zone and their discretization by a histogram with n_{V_∞} number of bins. [Colour figure can be viewed at wileyonlinelibrary.com]

variance of the resulting $f(\mathbf{V}_{\text{CFD}}; \mathbf{x})$ are given by

$$\bar{\mathbf{V}}_{\text{CFD}}(\mathbf{x}) = \sum_{k=1}^{n_{V_\infty}} f(V_\infty(k); \mathbf{x}) \mathbf{V}_{\text{CFD}}(V_\infty(k), \mathbf{x}) \quad (1)$$

$$\sigma_{\mathbf{V}_{\text{CFD}}}^2(\mathbf{x}) = \sum_{k=1}^{n_{V_\infty}} f(V_\infty(k); \mathbf{x}) [\mathbf{V}_{\text{CFD}}(V_\infty(k), \mathbf{x}) - \bar{\mathbf{V}}_{\text{CFD}}(\mathbf{x})]^2 \quad (2)$$

These measures can be compared directly with the corresponding ones of $f(\mathbf{V}; \mathbf{x})$ to evaluate the validity of the CFD model. The centre of each k^{th} bin is given by

$$V_\infty(k) = V_\infty^{\min} + \frac{V_\infty^{\max} - V_\infty^{\min}}{n_{V_\infty}} \left(k - \frac{1}{2} \right) \quad (3)$$

In this equation, $k = 1, 2, \dots, n_{V_\infty}$, where V_∞^{\min} and V_∞^{\max} represent the boundaries of free-stream velocities over which the validation is performed. The reconstruction of a distribution from a histogram is also known as the *simple histogram method*. This method originated from simulating dispersion with steady-state RANS and is commonly used to incorporate the stochastic variability of wind direction over time.^{7,8} The advantage of combining time-invariant solutions is the possibility of using simpler RANS models in combination with an actuator disc for numerically solving the flow. A more accurate model would not necessarily yield any better results, as the larger uncertainty in the model inputs would conceal any gain in accuracy in the outputs. The fundamental improvement this method provides is the independence of the validation from any kind of data sorting process—usually done in time and/or for wind speeds—which increases the confidence in the validation itself. Additionally, it allows for the use of all acquired data at once and avoids splitting measurements into smaller subsets, thus using the available data fully. Another important feature is the complete decoupling of experimental and numerical methods, as the numerical model does not use any other input from the measurements apart from the free-stream velocity. As a consequence, the model is not fitted to the measurements; instead, the boundary conditions are matched. Note that an essential part to this methodology is the estimation of the free-stream time series, which will be discussed in Section 4.4.

3. DATA PROCESSING OVERVIEW

A triple-lidar captures complex flow patterns over large areas, bringing with it added complexity in its data analysis, especially in terms of uncertainty quantification. This is reflected in the coming sections. Therefore, Figure 4 shows the connection between different processes that correspond to certain sections of this paper. The processes are either associated with the triple-lidar or the CFD model and grouped accordingly into Sections 4 and 5.

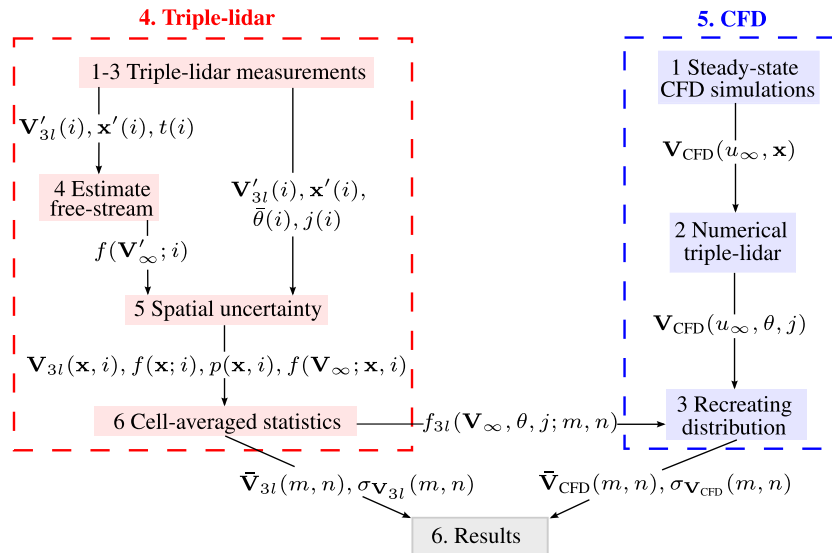


Figure 4. Validation process chain. Each process is outlined in the section denoted by the number in each block. [Colour figure can be viewed at wileyonlinelibrary.com]

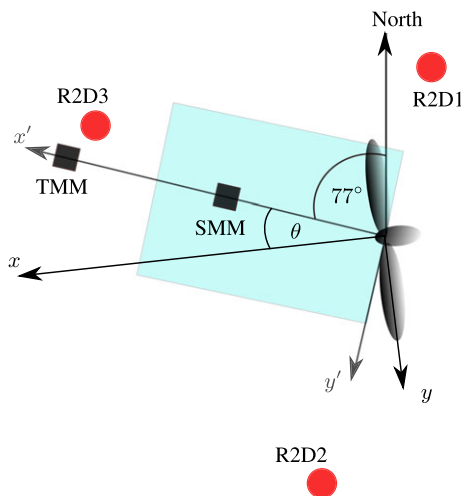


Figure 5. Schematic of the experimental setup. ● = lidars; ■ = met masts (T = tall, S = short); shaded rectangle = lidar scanning area. The triple-lidar measurements are misaligned with the rotor by θ . [Colour figure can be viewed at wileyonlinelibrary.com]

4. TRIPLE-LIDAR

4.1. Experimental setup

4.1.1. Measurement layout.

The Nordtank NTK 500 wind turbine is located at the southern edge of the DTU Risø campus, just off the Roskilde Fjord (N $55^\circ 41' 04''$, E $012^\circ 05' 48''$). The triple-lidar coordinate system had the turbine's base at its origin. Its x -axis was aligned with the prevailing wind direction of 283° , passing through both the tall and short met masts (TMM/SMM). Coming from this direction, the flow passes from fjord to land, up a gentle slope. The overall layout is pictured schematically in Figure 5. The exact coordinates of all instruments are listed in Table I. The TMM was equipped with several instruments along its entire height of 57 m, whereas the SMM only had a sonic anemometer at its tip of 30.5 m. The triple-lidar scanning pattern sliced the induction zone horizontally at hub height (36 m), covering the entire rotor diameter. The prescribed scanning trajectory thus encompassed a plane of $64 \text{ m} \times 40 \text{ m}$ ($3.1R \times 2.0R$) and took 15 s to complete, as shown in Figure 6. The

Table 1. Coordinates of instrument locations.

	x' [m]	y' [m]	z' [m]
NTK	0.00	0.00	0.00
R2D1	-0.94	-34.6	0.60
R2D2	-1.01	49.6	2.09
R2D3	78.7	5.40	-0.75
SMM	46.8	0.12	-1.61
TMM	92.00	-0.23	-3.03

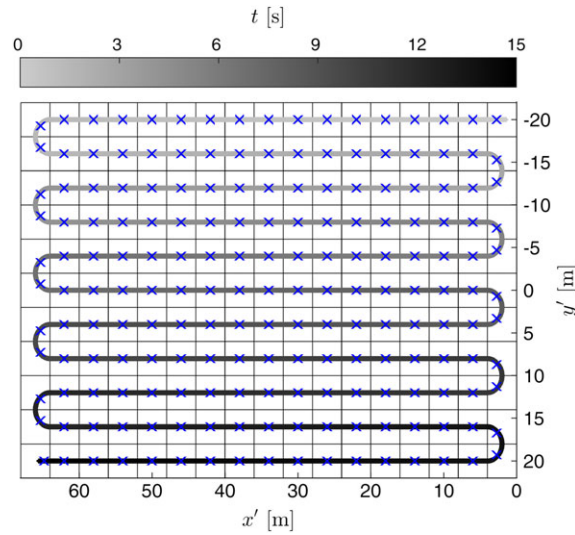


Figure 6. Triple-lidar grid and sampling path. x = Cell - averaged points. [Colour figure can be viewed at wileyonlinelibrary.com]

trajectory was fixed during the entire experiment and was thus misaligned with the rotor at times by an angle θ . As in the measurements performed by Simley,⁶ the lidars were positioned, such that their line-of-sight would intersect the main wind vector far from perpendicular and minimize their probe volumes.

4.1.2. Nordtank NTK 500/41.

The stall-regulated turbine is equipped with three 20.5 m blades and has a hub height of 36 m. The turbine is operational between wind speeds of 4 and 25 m/s and maximally generates 500 kW. Under these conditions, the rotor performs approximately 27.0 rotations per minute (rpm). Strain gauges and accelerometers are located at several points along the main shaft, blades and tower. For a more detailed description of the sensory equipment and the turbine, see Hansen *et al.*⁹ All sensors, including the yaw sensor, were calibrated prior to the experiment.¹⁰

4.2. Doppler spectra processing

The lidars sample the backscattered light signal at 100 MHz and compute 2×10^5 Doppler spectra per second by fast Fourier transformation. Each spectrum is split into 256 frequency bins, with a Nyquist frequency of 50 MHz the bin width corresponds to $\Delta f = 195$ kHz. The velocity step for each bin is directly related to it by $\Delta v_{los} = \frac{1}{2} \Delta f \lambda = 0.153$ m/s, where $\lambda = 1.56 \mu\text{m}$ represents the laser wavelength. So as to increase the signal-to-noise ratio, all 1.6×10^4 Doppler spectra falling into one $4 \text{ m} \times 4 \text{ m}$ cell were averaged (Figure 6). As a result, only a single v_{los} remained per lidar and cell. An ideal scan therefore contained 187 data points. The exact procedure to derive velocities from lidar Doppler spectra, including various filtering operations, is outlined in detail by Angelou *et al.*^{11,12} The volume-averaged estimates of the velocity components in each cell can be found from the v_{los} in combination with the beam direction unit vectors as described by Simley.⁶ Despite the filtering operations at a spectral level some erroneous measurements remained in the velocity data. A gradient-based spike detection algorithm¹³ was used in combination with manual filtering, removing on average 2% and maximally 3% of the data points. Denoting the triple-lidar by $3l$ and the measurement point index by i , the velocity vector at location $\mathbf{x}'(i)$ and time $t(i)$ is $\mathbf{V}'_{3l}(i)$.

4.3. Lidar measurement summary

Over 11 days, 11.5 h of data were acquired. The turbine was operational during 5 h of these measurements, and only those were considered in the following analyses, totalling 197×10^3 valid triple-lidar points. A summary of the meteorological conditions during each 30 min measurement period is presented in Table II. For further background, information on the measurement campaign and its methods consult the UniTTe reports^{10,14} and for a full description of the triple-lidar measurement system refer to Mikkelsen.¹⁵

4.4. Estimating the free-stream velocity probability density function

Usually velocity data from the TMM would be considered representative of the free-stream. However, its signal suffers from decorrelation with some of the cells in the triple-lidar grid. With a strong cross-flow, relative to the experimental setup, a gust encountered at the TMM for instance might not be encountered by any of the triple-lidar cells. Another important factor is the varying time-lag between the met mast and the triple-lidar velocity signal. Therefore, the triple-lidar data themselves are used to determine the spatial and temporal variation of the free-stream velocity. The idea is to derive the free-stream conditions in all 187 grid cells of each triple-lidar scan from measurements taken furthest from the rotor; as there, the induced velocities are lowest. As the estimation process is in itself uncertain the free-stream velocity is treated as a stochastic process. Thus, each triple-lidar data point is associated with a unique free-stream velocity pdf. An added benefit over a deterministic approach is that it mediates the impact of assumptions made in the validation methodology.

Table II. Summary of the usable 30 min triple-lidar measurement periods with a total of 1117 trajectory scans comprising 197×10^3 valid triple-lidar points.

#	Date [dd/mm]	Start time [hh:mm]	\bar{v}_∞ [m/s]	TI [%]	WD [°]
1	06/08	08:16	3.89	13.6	298
2	20/08	12:26	10.3	10.6	255
3	21/08	10:17	7.39	14.0	246
4	25/08	10:40	6.06	13.8	249
5	27/08	08:03	5.39	13.2	292
6	25/09	09:35	9.59	11.3	271
7	27/09	12:11	9.49	14.1	275
8	27/09	13:50	8.43	11.1	274
9	27/09	15:28	8.16	12.1	277
10	02/10	14:01	2.64	9.96	282

The values in the 4th–6th column were determined from the large met mast at hub height and denote: mean wind speed, turbulence intensity and wind direction. Note that the scanning trajectory was fixed and aligned with a wind direction of 283° .

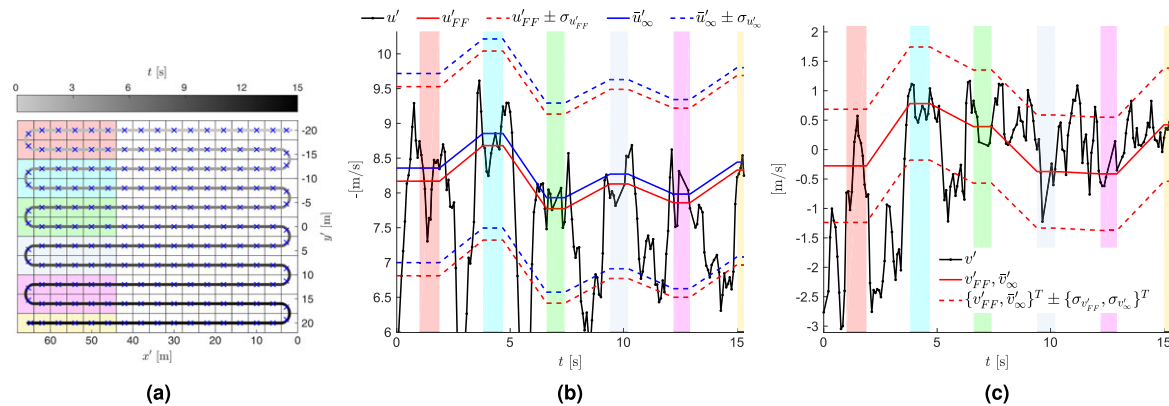


Figure 7. A visual representation of the far-field velocity estimation. (a) Triple-lidar scan trajectory with colour coded averaging areas; (b) Axial velocity u for a triple-lidar scan shown in (a) with various far-field estimates and same colour coded averaging areas; (c) As (b) only for the radial velocity component v . [Colour figure can be viewed at wileyonlinelibrary.com]

The latter implicitly assumes that the free-stream velocity in one cell instantaneously determines the thrust and thus the upstream flow-field. However, with a stochastic representation weight is given to a range of free-stream velocities softening the instantaneity requirement. Similarly, it could be interpreted as a variation of the free-stream velocity along the radial direction. The method for approximating the pdf is outlined in the following subsections and supported by Figure 7.

4.4.1. Velocity far from rotor.

The triple-lidar measures solely six times during a single scan far from the rotor (Figure 7(a)), making a continuous far-field estimate for all 187 cells difficult. Essentially, it corresponds to estimating the signal from a second triple-lidar scanning simultaneously along $x \approx 3R$. The approach here relies on establishing averaging areas far from the rotor, shown in different colours in Figure 7(a). All velocity measurements falling into one of these areas are averaged and assumed to be representative of the far-field conditions in each respective averaging area. Here, spatially averaging avoids bias from a single point estimate. The estimated mean far-field velocity $\mathbf{V}'_{FF} = \{u'_{FF}, v'_{FF}, w'_{FF}\}$ is thus constant over these areas, which is shown in Figure 7(b) and 7(c) for the axial and radial velocity components. By interpolating between these regions, all cells are attributed a far-field velocity. Note that cells lying in front of the first averaging area (red) in time are assigned its average value.

4.4.2. Uncertainty from wind variability.

As the rotor induction zone might interact with the ambient turbulence, the standard deviation is also estimated in the far-field. For each of the cells falling into the coloured averaging areas, the standard deviation is determined over each of the continuous 30 min triple-lidar acquisition periods. The average of all their standard deviations is then taken as the final standard deviation of the far-field velocity $\sigma_{\mathbf{V}'_{FF}} = \{\sigma_{u'_{FF}}, \sigma_{v'_{FF}}, \sigma_{w'_{FF}}\}$. Note that this signifies that each of the ten 30 min triple-lidar measurement periods has only one far-field standard deviation associated with it. It does not vary in space, as this has shown to be insignificant. The resulting far-field estimates are again shown in Figure 7(b) and 7(c).

4.4.3. Estimating the induced velocity.

The axial velocity induced by the rotor is still significant at the position where the triple-lidar far-field velocity is estimated. The latter should be corrected by the rotor induced velocity to obtain a better estimate of the ‘true’ free-wind speed. The induced velocity is estimated by calculating the induction of a cylindrical vortex sheet trailed from the rotor tip and extending infinitely far downstream. Along the centreline of such a vortex system, the induced velocity is given by:⁴

$$u_I = \frac{1}{2} \left(1 - \sqrt{1 - C_T} \right) u_{\infty} g(x) \quad (4)$$

$$g(x) = \left(1 - \frac{x}{\sqrt{R^2 + x^2}} \right) \quad (5)$$

where C_T is the thrust coefficient. The aforementioned expression for the induced velocity is uncertain owing to the crude assumptions behind the model as well as the uncertainties in predicting C_T and u_{∞} . In order to quantify this uncertainty, the measured C_T of the NTK 500 is first approximated by the following expression:

$$C_T = 1 - (b_2 u_{\infty} + b_1)^2 \quad (6)$$

where $b_2 = 0.055$ s/m and $b_1 = 0.079$ are determined using least-squares fitting. A detailed discussion of the measured thrust curve is given in Section 6.1. Figure 8 shows a good fit over the wind speed range for which measurements are available. For us to avoid an iterative process, the dependence of u_I on u_{∞} is removed by assuming $u_{\infty} \approx u'_{FF}$. The combined equations (4)-(6) yield

$$u_I = (c_2 u'_{FF} + c_1) u'_{FF} g(x) \quad (7)$$

where $c_2 = -\frac{1}{2} b_2 = -0.028$ s/m and $c_1 = \frac{1}{2} (1 - b_1) = 0.46$. Assuming $u_{\infty} \approx u'_{FF}$ causes the term between brackets in equation (7) to increase and the one outside to decrease and therefore should not affect the estimate of u_I significantly. Next, it is assumed that u'_{FF} , c_1 and c_2 are independent random variables. Linearizing around the most likely u_I then yields:

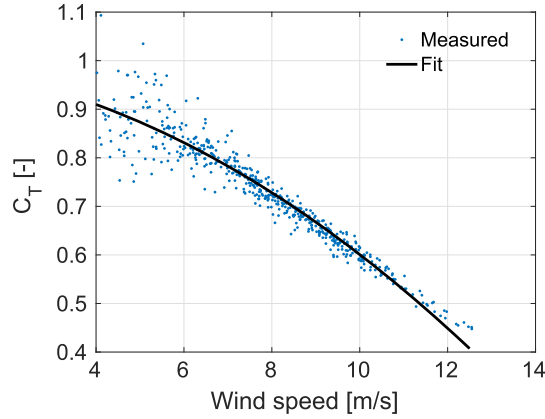


Figure 8. Comparison of measured C_T and the fit given by equation (6). [Colour figure can be viewed at wileyonlinelibrary.com]

$$\sigma_{u_I}^2 = \left(\frac{\partial u_I}{\partial u'_{FF}} \right)^2 \sigma_{u'_{FF}}^2 + \left(\frac{\partial u_I}{\partial c_1} \right)^2 \sigma_{c_1}^2 + \left(\frac{\partial u_I}{\partial c_2} \right)^2 \sigma_{c_2}^2 \quad (8)$$

where $\sigma_{c_2} = 6.7 \cdot 10^{-4}$ s/m and $\sigma_{c_1} = 6.0 \cdot 10^{-3}$ are determined by the least square procedure. The standard deviation of u'_{FF} is in the order of 1 m/s that is significantly higher than σ_{c_2} and σ_{c_1} . Thus, the last two terms in equation (8) can be neglected, i.e.

$$\left(\frac{\sigma_{u_I}}{\sigma_{u'_{FF}}} \right)^2 \approx \left(\frac{\partial u_I}{\partial u'_{FF}} \right)^2 = ((2c_2 u'_{FF} + c_1)g(x))^2$$

At $x \approx 3R$, the function $g(x) \approx 0.05$ and hence $\sigma_{u_I}^2 \approx \left((-2.8 \cdot 10^{-3} u'_{FF} + 0.023) \sigma_{u'_{FF}} \right)^2$. Thus, the uncertainty in the estimated u_I is only a small fraction of the variability of u'_{FF} .

4.4.4. Forming the free-stream pdf.

Finally all contributions from the last sections can be combined to form the basis of the free-stream pdf

$$\bar{\mathbf{V}}'_\infty = \begin{bmatrix} \bar{u}'_\infty \\ \bar{v}'_\infty \\ \bar{w}'_\infty \end{bmatrix} = \begin{bmatrix} u'_{FF} + u_I \\ v'_{FF} \\ w'_{FF} \end{bmatrix} \quad \sigma_{\mathbf{V}'_\infty} = \begin{bmatrix} \sigma_{u'_\infty} \\ \sigma_{v'_\infty} \\ \sigma_{w'_\infty} \end{bmatrix} = \begin{bmatrix} \sqrt{\sigma_{u'_{FF}}^2 + \sigma_{u_I}^2} \\ \sigma_{v'_{FF}} \\ \sigma_{w'_{FF}} \end{bmatrix} \quad (9)$$

Their time-series are shown Figure 8(b) and 8(c). The free-stream pdf of each i^{th} data point in the triple-lidar coordinate system thus becomes

$$f(\mathbf{V}'_\infty; i) = \mathcal{N}(\bar{\mathbf{V}}'_\infty(i), \sigma_{\mathbf{V}'_\infty}(i)) \quad (10)$$

Here, \mathcal{N} defines a Gaussian distribution.

4.5. Spatial uncertainty in triple-lidar data

The induction zone is only a function of the rotor frame of reference, however even with the rotor following the wind the triple-lidar measurements followed a fixed pattern (Section 4.1). The yaw sensor of the NTK 500/41 provided an indication of the mean misalignment between the measured and rotor coordinate system $\bar{\theta}$. Nevertheless, the turbine controller employs a yaw margin to avoid wearing down the yaw system, introducing uncertainty in the misalignment angle. The rotor and triple-lidar coordinate systems are related via the transformation matrix $T(\theta)$ such that $\Psi = T(\theta)\Psi'$.

$$T(\theta) = \begin{bmatrix} \cos(\theta) & \sin(\theta) \\ -\sin(\theta) & \cos(\theta) \end{bmatrix} \quad (11)$$

Therefore, the uncertainty in θ propagates to the location of the measurements and their velocity components in Ψ . The uncertainty in the misalignment is modelled via $\mathcal{N}(\bar{\theta}(i), \sigma_\theta)$, a Gaussian distribution with $\sigma_\theta = 5^\circ$, based on the calibration report¹⁰ and work by Kragh *et al.*¹⁶ The resulting mean misalignment is shown in Figure 9 with $\pm\sigma_\theta$ for all triple-lidar data

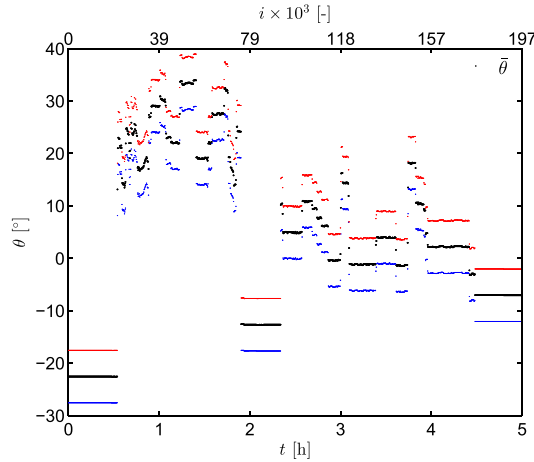


Figure 9. Triple-lidar-rotor misalignment for all triple-lidar data points. The lower axis indicates the cumulative time, the upper the data point index. Coloured points indicate σ_θ boundaries about the mean. [Colour figure can be viewed at [wileyonlinelibrary.com](#)]

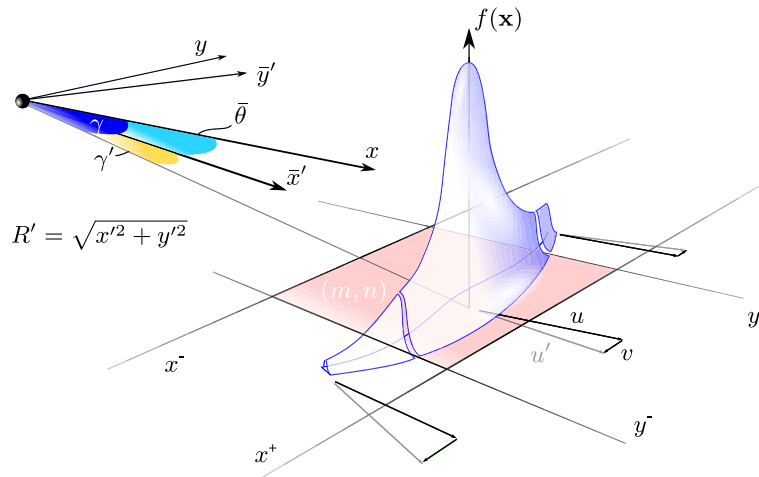


Figure 10. Spatial weighting of a single triple-lidar data point. [Colour figure can be viewed at [wileyonlinelibrary.com](#)]

points. Defining $\gamma = -\tan^{-1}(y/x)$ and $\gamma'(i) = -\tan^{-1}(y'(i)/x'(i))$, the pdf for each data point i in the rotor coordinate system becomes

$$f(\gamma; i) = \mathcal{N}([\bar{\theta}(i) + \gamma'(i)], \sigma_\theta) \tag{12}$$

Furthermore, the triple-lidar cell-averaged data should not be perceived as discrete points in space, owing to the uncertainty in the scan trajectory. The standard deviation in $R'(i) = \sqrt{x'(i)^2 + y'(i)^2}$ was 0.11 m. Again, the pdf was modelled as a normal

$$f(R; i) = \mathcal{N}(R'(i), \sigma_{R'}) \tag{13}$$

, where $R = \sqrt{x^2 + y^2}$. Finally, the total spatial uncertainty is

$$f(\mathbf{x}; i) = f(\gamma; i)f(R; i) \tag{14}$$

A visual representation of a single data point’s pdf and the different angles defined earlier is given in Figure 10. It further demonstrates the effect of the uncertainty in the reference frame misalignment on the rotor velocity components, indicated by the arrows. Here, a u' component with a misalignment $\bar{\theta}$ gives rise to both velocity components in the rotor reference frame. The uncertainty in θ furthermore changes the velocity components in space. The entire rotor velocity field under

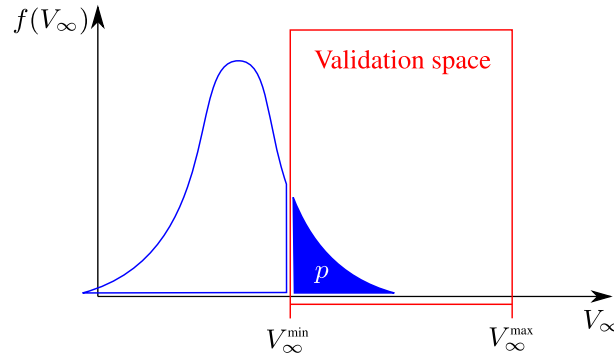


Figure 11. Evaluation of the participation of a single triple-lidar measurement at some point in space. Note $\bar{V}_\infty(i) < V_\infty^{\min}$. [Colour figure can be viewed at wileyonlinelibrary.com]

uncertainty in the misalignment angle can be computed from the triple-lidar signal

$$\begin{bmatrix} u_{3l}(\gamma, i) & \bar{u}_\infty(\gamma, i) & \sigma_{u_\infty}(\gamma, i) \\ v_{3l}(\gamma, i) & \bar{v}_\infty(\gamma, i) & \sigma_{v_\infty}(\gamma, i) \end{bmatrix} = T(\gamma - \gamma'(i)) \begin{bmatrix} u'_{3l}(i) & \bar{u}'_\infty(i) & \sigma_{u'_\infty}(i) \\ v'_{3l}(i) & \bar{v}'_\infty(i) & \sigma_{v'_\infty}(i) \end{bmatrix} \quad (15)$$

$$\begin{bmatrix} w_{3l}(\gamma, i) \\ \bar{w}_\infty(\gamma, i) \\ \sigma_{w_\infty}(\gamma, i) \end{bmatrix} = \begin{bmatrix} w'_{3l}(i) \\ \bar{w}'_\infty(i) \\ \sigma_{w'_\infty}(i) \end{bmatrix} \quad (16)$$

Note that $\theta(\mathbf{x}, i) = \gamma - \gamma'(i)$. This finally gives a rotor velocity field for each data point $\mathbf{V}_{3l}(\mathbf{x}, i)$ but also a spatially varying free-stream pdf.

$$f(\mathbf{V}_\infty; \mathbf{x}, i) = \mathcal{N}(\bar{\mathbf{V}}_\infty(\mathbf{x}, i), \sigma_{\mathbf{V}_\infty}(\mathbf{x}, i)) \quad (17)$$

The velocity range over which the validation is performed is linked to the turbine's operating wind speeds. This implies that some triple-lidar measurements only participate in the comparison by a factor given as

$$p(\mathbf{x}, i) = \int_{V_\infty^{\min}}^{V_\infty^{\max}} f(V_\infty; \mathbf{x}, i) dV_\infty \quad (18)$$

Figure 11 shows the participation of a single triple-lidar point with a free-stream pdf where $\bar{V}_\infty(i) < V_\infty^{\min}$.

4.6. Cell-averaged statistics

Finally, all triple-lidar data can be gathered in space and time forming a pdf. The spatial integration of the uncertainty is performed numerically by discretizing the x - y plane with a spacing $\Delta x = \Delta y = 0.04$ m over $0 \text{ m} \leq \Delta x \leq 68$ m and $-22 \text{ m} \leq y \leq 22$ m. The upper and lower spatial boundaries of each grid cell (m, n) (Figure 10), denoted by the superscripts $+$ and $-$, followed from the original triple-lidar grid shown in Figure 6. Over a discretized cell, the spatial coordinates become

$$\begin{aligned} \Delta x &= \frac{x^+(m, n) - x^-(m, n)}{n_x} & \Delta y &= \frac{y^+(m, n) - y^-(m, n)}{n_y} \\ x_r &= x^-(m, n) + (r - \frac{1}{2})\Delta x & y_s &= y^-(m, n) + (s - \frac{1}{2})\Delta y \end{aligned}$$

Here, n_\bullet denotes the total number of points discretizing each dimension. Consequently, the mean and variance of a triple-lidar velocity pdf $f(\mathbf{V}_{3l}; m, n)$ in a cell (m, n) are given by

$$\bar{\mathbf{V}}_{3l}(m, n) = \frac{\sum_{r=1}^{n_x} \sum_{s=1}^{n_y} \left(\sum_{i=1}^{n_{3l}} \mathbf{V}_{3l}(\mathbf{x}_{rs}, i) f(\mathbf{x}_{rs}; i) p(\mathbf{x}_{rs}, i) \right)}{\sum_{r=1}^{n_x} \sum_{s=1}^{n_y} \left(\sum_{i=1}^{n_{3l}} f(\mathbf{x}_{rs}; i) p(\mathbf{x}_{rs}, i) \right)} \quad (19)$$

$$\sigma_{V_{3l}}^2(m, n) = \frac{\sum_{r=1}^{n_x} \sum_{s=1}^{n_y} \left(\sum_{i=1}^{n_{3l}} [\mathbf{V}_{3l}(\mathbf{x}_{rs}, i) - \bar{\mathbf{V}}_{3l}(m, n)]^2 f(\mathbf{x}_{rs}; i) p(\mathbf{x}_{rs}, i) \right)}{\sum_{r=1}^{n_x} \sum_{s=1}^{n_y} \left(\sum_{i=1}^{n_{3l}} f(\mathbf{x}_{rs}; i) p(\mathbf{x}_{rs}, i) \right)} \quad (20)$$

The free-stream distributions in each cell needed for the CFD reconstruction is more complex compared with the one presented in Section 2, owing to the intrinsic cell-averaging of the triple-lidar data. The triple-lidar acquires spectra along some path $\mathbf{x}'(t)$ (Figure 6) at a misalignment of $\theta(t)$ - assuming it is exactly known—which are subsequently averaged over a grid cell j to determine a cell velocity (Section 4.1). The latter can be expressed in terms of the ‘true’ wind field $\mathbf{V}(V_\infty, \mathbf{x}, t)$, ignoring volume-averaging

$$\mathbf{V}_{3l}(i) = \frac{1}{\delta t(j(i))} \int_{t(i)-\delta t(j(i))/2}^{t(i)+\delta t(j(i))/2} \mathbf{V}(\overbrace{T(\theta(t))V_\infty}'(t), \overbrace{T(\theta(t))\mathbf{x}'(t), t}^{\mathbf{x}(t)}) dt \quad (21)$$

The limits of the integral are given by the time of the measurement and the time span the triple-lidar focal point rests in a particular grid cell. This implies that each lidar measurement does not solely depend V_∞ but also on the triple-lidar grid cell j and misalignment θ . Hence, for recreating the measurements from the true wind field (or equivalently the CFD solution), an estimated pdf needs to capture these additional dependencies. Noting that the spatially weighted free-stream pdf $f(\mathbf{V}_\infty; \mathbf{x}, i)f(\mathbf{x}; i)$ is linked to $\theta(\mathbf{x}, i)$ and $j(i)$ via the data index i , a multi-dimensional joint pdf can be formed from all data that captures these dependencies stochastically

$$f_{3l}(\mathbf{V}_\infty, \theta, j; \mathbf{x}) \quad (22)$$

Treating the pdf as fully discrete and integrating it spatially over the cell (m, n) yields the final pdf used for recreating the measurements, detailed in Section 5.3.

$$f_{3l}(\mathbf{V}_\infty, \theta, j; m, n) = \frac{\sum_{r=1}^{n_x} \sum_{s=1}^{n_y} f_{3l}(\mathbf{V}_\infty, \theta, j; \mathbf{x}_{rs})}{\sum_{r=1}^{n_x} \sum_{s=1}^{n_y} \sum_{k=1}^{n_{V_\infty}} \sum_{l=1}^{n_\theta} \sum_{r=1}^{n_j} f_{3l}(\mathbf{V}_\infty, \theta, j; \mathbf{x}_{rs})} \quad (23)$$

Note that the normalization should be performed for each velocity component individually.

5. COMPUTATIONAL METHOD

5.1. CFD simulations

5.1.1. Numerical setup.

The simulations were performed using incompressible steady-state RANS with sheared inflow and an actuator disc representation of the rotor.¹⁷ The kinematic viscosity and air density were kept constant at 1.789×10^{-5} kg/m³ and 1.225 kg/m³, respectively. Neither nacelle nor tower were modelled. Only the velocity prescribed at the inlet boundary \mathbf{V}_∞ changed between calculations. It was varying with height according to a rough logarithmic velocity profile (log-law), where the roughness length z_0 was determined from fitting the profile to wind speeds measured at three different heights of the TMM, resulting in $z_0 = 0.055$. This corresponds to the terrain category of the site for the wind directions of interest, i.e. *farmland with open appearance*.¹⁸ The friction velocity followed from specifying the free-stream velocity at hub height $\mathbf{V}_{\infty, h}$. It corresponds to the velocity of the k th bin used to discretise f_{3l} , as given in equation (3). The small magnitude and large uncertainty in v_∞ and w_∞ meant that only u_∞ was used as input to the simulations, such that $\mathbf{V}_{\infty, h} = \{u_\infty(k), 0, 0\}$. The crudity of the numerical representation was not expected to undermine the accuracy of the numerical results, as this numerical setup also yields accurate results for the wake deficit of a rotor.^{19,20} The wake deficit is, as the induction zone, governed by the turbine’s thrust.

5.1.2. Flow solver.

The in-house finite volume code EllipSys3D solves the incompressible RANS equations over a discretised block-structured domain.^{21–23} The QUICK scheme²⁴ is applied to the convection-diffusion equation. It is third order accurate by using quadratic interpolation over three nodes. The SIMPLE algorithm²⁵ solves the pressure-linked terms by coupling the

Navier–Stokes equations in an iterative manner. The discrete body forces from the actuator disc are hindered by a modified Rhie–Chow algorithm from decoupling velocity and pressure.^{26,27} The Menter $k - \omega$ shear-stress transport closes the RANS equations.²⁸

5.1.3. Numerical domain.

A box domain with side lengths of 25 radii (R) was created, minimizing the impact of domain blockage ($\pi/25^2 = 0.5\%$). The actuator disc was located at the NTK hub height (Figure 12) and was surrounded by a finely meshed box with $2.5R$ side lengths. The inner mesh resolution followed from discretizing the rotor radius with 33 grid points, which has been shown in previous studies to yield sufficiently accurate results.^{19,29} From the fine mesh, the grid grew hyperbolically towards the edges of the domain. The front, sides and top boundaries of the domain were prescribed according to the specified shear profile (Dirichlet), while the outlet was a Neumann boundary. The bottom face was set as no-slip boundary with a roughness length of $z_0 = 0.055$.

5.2. Numerical triple-lidar

For us to make the simulation results more comparable with the measured data, the simulated flow was sampled by a numerical triple-lidar. Each of the three continuous-wave lidars in fact probes the flow-field along the entire length of its laser beam and not in a single point. This phenomenon is also referred to as volume averaging or range weighting. A detailed modelling approach is given by Simley *et al.*⁶ The numerical triple-lidar followed the same measurement trajectory as the real one shown in Figure 6, and the sampled velocities are spatially averaged in similar fashion. Furthermore, the

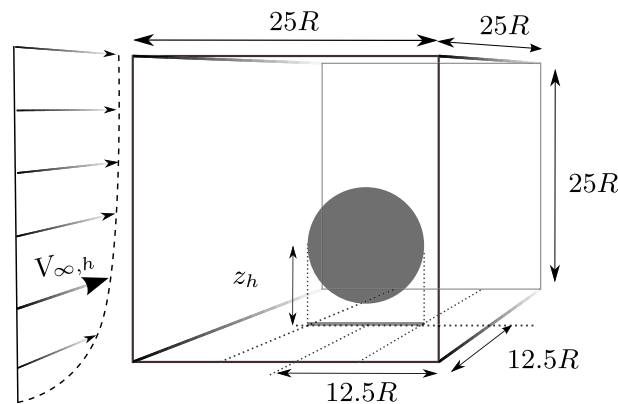


Figure 12. The numerical domain containing the actuator disc with sheared inflow and a free-stream velocity at hub height $V_{\infty,h} = u_{\infty}(k)$. All dimensions are given in turbine radii ($R = 20.5$ m).

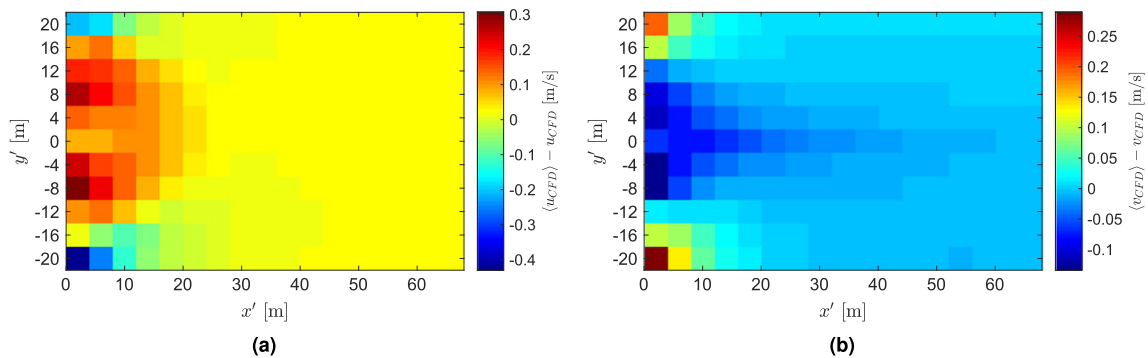


Figure 13. The difference between volume-averaged and point-like sampled a) axial b) radial CFD velocity fields. The results are furthermore cell-averaged. The free-stream velocity at hub height is 5 m/s, $\theta = 0$ and the sheared inflow followed a log-law. [Colour figure can be viewed at wileyonlinelibrary.com]

fixed measurement coordinates necessitate sampling the flow over trajectories at various angles θ (Figure 5) to the rotor coordinate system. This was performed in-between -44° and 54° in 1° steps. This impacts the final comparison, as with a non-zero θ the flow is no longer sampled at right angles to the rotor plane. Finally, the CFD velocity field is a function of the free-stream velocity u_∞ , the misalignment angle θ and j , the grid cell index, i.e. $\mathbf{V}_{\text{CFD}}(u_\infty, \theta, j)$. For a free-stream velocity at hub height of 5 m/s and $\theta = 0$, the difference between numerical triple-lidar velocities and point-like velocity data is shown in Figure 13. Close to the rotor $x < 1.5R$ volume-averaging becomes significant, as gradients are smeared out by the lidar's range-weighting.

5.3. Recreating the free-stream velocity distribution

Discretizing $f_{3l}(\mathbf{V}_\infty, \theta, j; m, n)$ over the sample-space, the modelled statistics can be computed in combination with the CFD results extracted by the numerical triple-lidar. To clearly mark lidar and CFD contributions, they are denoted by \bullet_{3l} and \bullet_{CFD} .

$$\bar{\mathbf{V}}_{\text{CFD}}(m, n) = \sum_{k=1}^{n_{u_\infty}} \sum_{l=1}^{n_\theta} \sum_{r=1}^{n_j} f_{3l}(u_\infty(k), \theta(l), j(r); m, n) \mathbf{V}_{\text{CFD}}(u_\infty(k), \theta(l), j(r)) \quad (24)$$

$$\sigma_{\bar{\mathbf{V}}_{\text{CFD}}}^2(m, n) = \sum_{k=1}^{n_{u_\infty}} \sum_{l=1}^{n_\theta} \sum_{r=1}^{n_j} f_{3l}(u_\infty(k), \theta(l), j(r); m, n) [\mathbf{V}_{\text{CFD}}(u_\infty(k), \theta(l), j(r)) - \bar{\mathbf{V}}_{\text{CFD}}(m, n)]^2 \quad (25)$$

These equations only differ from those presented in Section 2 by the added variables θ, j and using u_∞ . Also note that for consistency $V_\infty(i) = u_\infty(i)$ in equation (18) to calculate the participation of the triple-lidar measurements. The effect of $v_{\infty,3l}$ is included in the CFD results by assuming that the induction zone behaves linearly to sufficiently small radial and vertical velocity components

$$\begin{bmatrix} \bar{v}_{\text{CFD},2} \\ \bar{w}_{\text{CFD},2} \end{bmatrix} = \begin{bmatrix} \bar{v}_{\text{CFD},1} + \bar{v}_{\infty,3l} \\ \bar{w}_{\text{CFD},1} + \bar{w}_{\infty,3l} \end{bmatrix} \quad \begin{bmatrix} \sigma_{v_{\text{CFD},2}}^2 \\ \sigma_{w_{\text{CFD},2}}^2 \end{bmatrix} = \begin{bmatrix} \sigma_{v_{\text{CFD},1}}^2 + \sigma_{v_{\infty,3l}}^2 \\ \sigma_{w_{\text{CFD},1}}^2 + \sigma_{w_{\infty,3l}}^2 \end{bmatrix} \quad (26)$$

Here, the subscript $_1$ denotes the result from equations (24) and (25), and $_2$ the final value that will be compared with the triple-lidar measurements.

6. RESULTS AND DISCUSSION

6.1. The thrust curve

As an initial validation of the computational method, the experimental and numerical global thrust coefficients were compared. The experimental data were derived from the tower bending moments as proposed by Réthoré.³⁰ The detailed

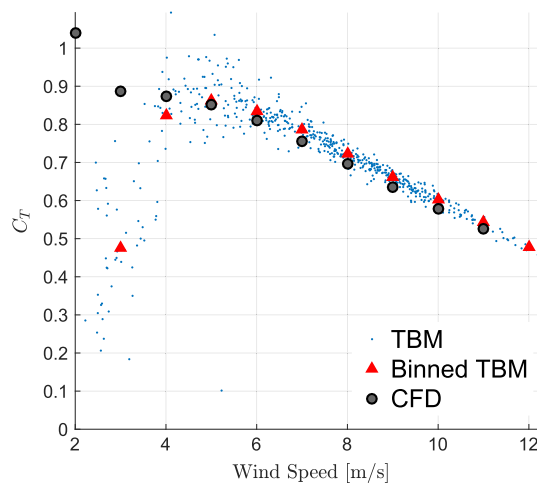


Figure 14. Thrust curves generated from tower bending moments (TBM) and RANS simulations with the actuator disc method. The wind speed is equivalent to the free-stream velocity at hub height. [Colour figure can be viewed at wileyonlinelibrary.com]

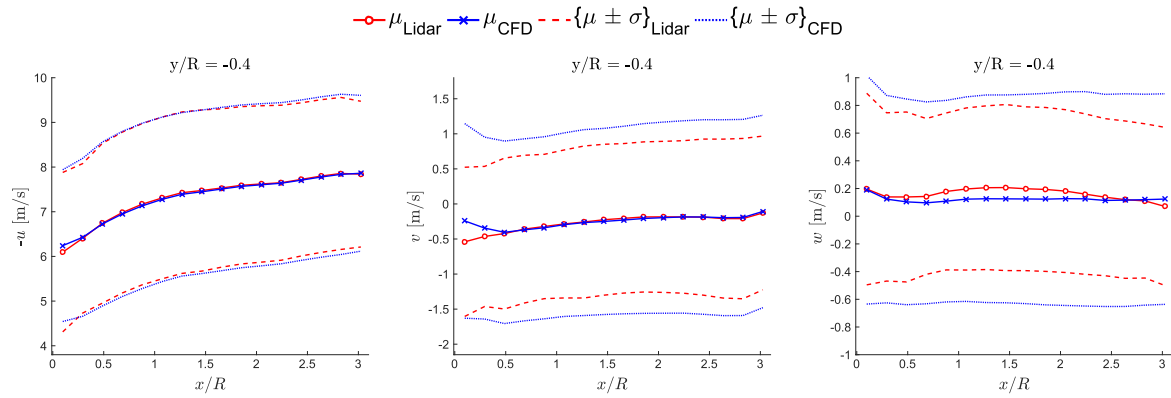
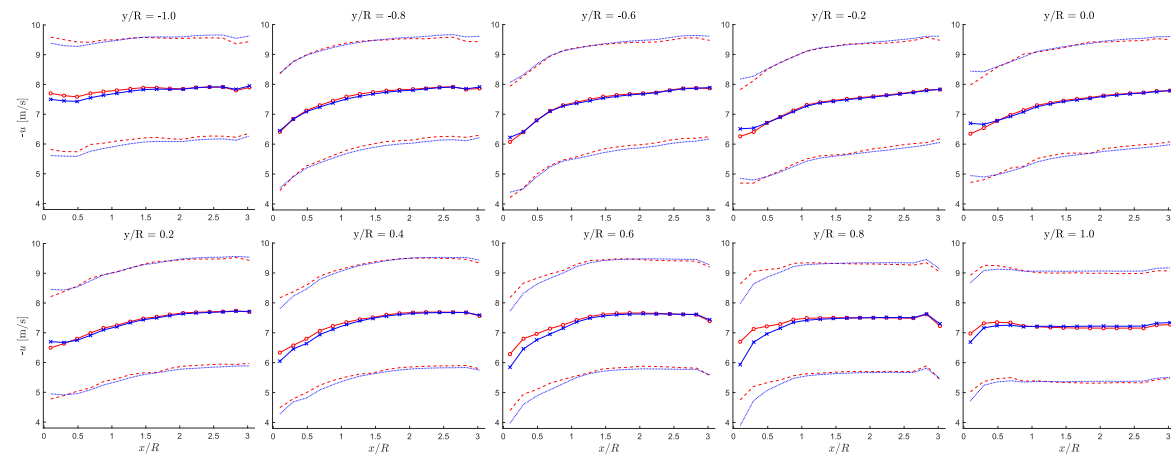
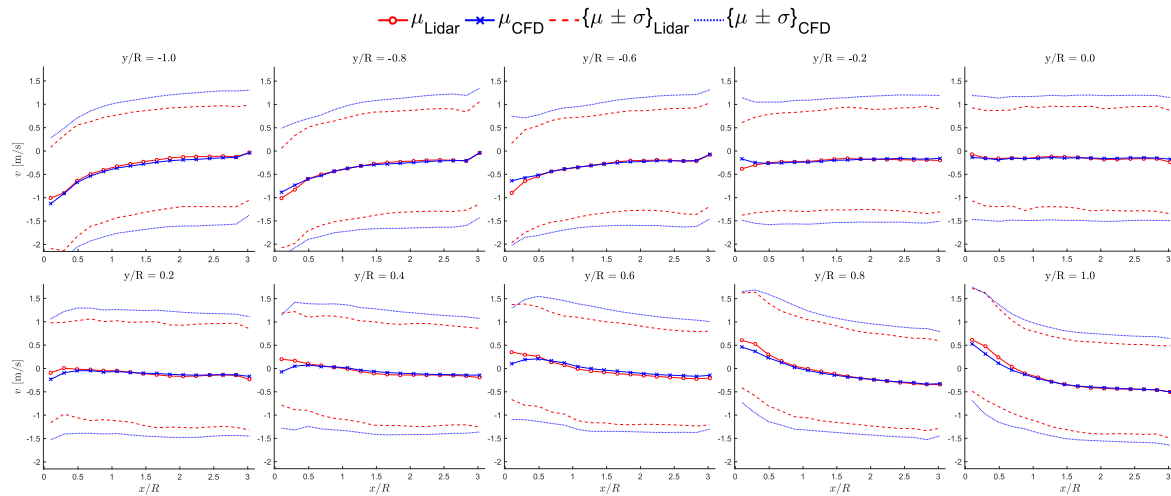


Figure 15. Comparison between mean μ and standard deviation σ of triple-lidar (o) and CFD (x) for all three velocities components $\{u, v, w\}$ along the line $(x/R, y/R = -0.4)$. [Colour figure can be viewed at wileyonlinelibrary.com]



(a) Axial velocity component



(b) Radial velocity component

Figure 16. Comparison between mean and standard deviation of triple-lidar(o) and CFD (x) along lines with constant y/R . [Colour figure can be viewed at wileyonlinelibrary.com]

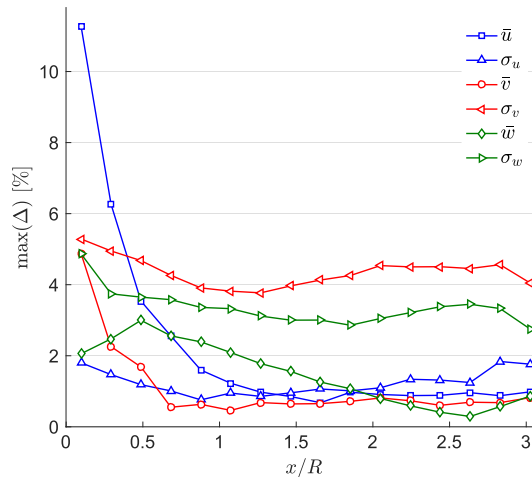


Figure 17. Maximal absolute difference across the rotor induction zone between triple-lidar and CFD statistics, normalised by the mean of the free-stream velocity in each cell. [Colour figure can be viewed at wileyonlinelibrary.com]

method can be found in the campaign report.¹⁰ Figure 14 demonstrates that the CFD simulations are in good agreement with the measurements over a large wind speed range. The best agreement was found for wind speeds > 5 m/s, as below this threshold, the turbine is barely running. This also causes the large scatter in the measurements. Figure 14 essentially verifies the RANS model for predicting the global thrust coefficient, under the condition that the free-stream velocity is matched. Consequently, the range of free-stream velocities in equation 3 over which the pdfs were discretized was set to $4.75 \text{ m/s} \leq u_\infty \leq 11.75 \text{ m/s}$ and with $n_{u_\infty} = 14$ the free-stream bin width was 0.5 m/s. Therefore, the CFD simulations were performed with 14 inlet velocities of $4.75 + 0.5(k - 0.5) \text{ m/s}$ with $k = 1, \dots, n_{u_\infty}$.

6.2. Comparison in the induction zone

Here, mean and standard deviations determined in Sections 4.6 and 5.3 for the triple-lidar measurements and CFD simulations are compared. Figure 15 shows these measures for all three velocity components along the line $(x/R, y/R = -0.4)$. These results are representative of the main features found across the entire validation space. The comparisons of u and v over the full rotor area are given in Figures 16a and 16b, respectively. Only when mean and standard deviation agree are the pdfs matching. This is the case for the u -component until close to the rotor, whereas for the radial velocity v , it is solely the mean. Its computed that standard deviation is larger. This over-prediction of σ_{v_∞} is directly linked to the free-stream estimate (equation 26), as $\sigma_{v_\infty} = \sigma_{v_\infty,3l}$, except for $x/R < 0.5$. Consequently, this difference is linked to estimating the inputs and cannot be attributed to model inaccuracies. The evolution of the vertical velocity w away from the rotor is not reproduced, as the simulations were performed for flat terrain. The maximal difference across the rotor between triple-lidar and CFD statistics are given in Figure 17 for all three velocity components. The results are normalized by \bar{V}_∞ in each cell. Except for σ_{v_∞} and statistics of w , the difference lies below 1.5% for $1 < x/R < 3$. It is really just for $x/R < 0.5$ that differences start to diverge. This might be related to the missing nacelle and tower in the simulations or the triple-lidar hitting hard targets.

7. CONCLUSION

Using a probabilistic approach that captures the variability of the wind field interacting with the rotor and the uncertainties in the field experiment allows to bring model and measurements in great accordance. The difference between triple-lidar and CFD statistics across the entire rotor induction zone lies below 4.5% up to half a radius upstream of the turbine relative to the measured free-stream velocity. For the axial component, it remains below 2% for $x/R > 0.8$, which translates into a maximal nominal difference of 0.14 m/s. This difference should be judged with respect to potential measurement errors. The minimal recorded standard deviation during a triple-lidar measurement period was almost double this figure at 0.26 m/s. The Doppler spectral resolution of the lidars lies at 0.15 m/s and a 1° error in the lidar beam angle would incur the same velocity difference. Essentially, this renders model and measurement errors indistinguishable, validating the model within the measurement error bounds. Close to the rotor its validity is more questionable, however, as both model and

measurements are suffering from errors in this region. The large uncertainties in the model inputs required a probabilistic approach to the validation, which obscures whether the model functions for specific scenarios. Here, field measurements are probably not the right choice, as neither inputs nor errors can be controlled. Wind tunnel measurements allow more control over the inputs and might allow to evaluate the performance of the model under different atmospheric conditions but might introduce scaling errors.

ACKNOWLEDGEMENTS

This work is part of the Unified Turbine Testing (UniTTe) project funded by The Innovation Fund Denmark (1305-00024B). Special thanks are due to the Test & Measurements section, in particular the WindScanner team, at DTU Wind Energy for their generous support as well as to R. Meyer Forsting for editing this document. Furthermore we would like to thank the anonymous reviewers for their valuable contribution. The computational resources were provided by the Risø DTU central computing facility.

REFERENCES

1. IEC 61400-12-1:2005, *power performance measurements of electricity producing wind turbines*.
2. Wagner R, Pedersen TF, Courtney M, Antoniou I, Davoust S, Rivera RL. Power curve measurement with nacelle mounted lidar. *Wind Energy* 2014; **17**: 1441–1453. DOI: 10.1002/we.1643.
3. Schlipf D, Fleming P, Haizmann F, Scholbrock AK, Hofsäß M, Wriugh A, Cheng PW. Field testing of feedforward collective pitch control on the cart2 using a nacelle-based lidar scanner. *Journal of Physics: Conference Series* 2012; **555**: 012090, DOI: 10.1088/1742-6596/555/1/012090.
4. Medici D, Ivanell S, Dahlberg JA, Alfredsson PH. The upstream flow of a wind turbine: blockage effect. *Wind Energy* 2011; **14**: 691–697. DOI: 10.1002/we.451.
5. Howard KB, Guala M. Upwind preview to a horizontal axis wind turbine: a wind tunnel and field-scale study. *Wind Energy* 2015; **19**: 1371–1389. DOI: 10.1002/we.1901.
6. Simley E, Angelou N, Mikkelsen T, Sjöholm M, Mann J, Pao LY. Characterization of wind velocities in the upstream induction zone of a wind turbine using scanning continuous-wave lidars. *Journal of Renewable and Sustainable Energy* 2016; **8**. DOI: 10.1063/1.4940025.
7. Quinn AD, Wilson M, Reynolds AM, Couling SB, Hoxey RP. Modelling the dispersion of aerial pollutants from agricultural buildings - an evaluation of computational fluid dynamics (CFD). *Computers and Electronics in Agriculture* 2001; **30**: 219–235.
8. Tang W, Huber A, Bell B, Schwarz W. Application of CFD simulations for short-range atmospheric dispersion over open fields and within arrays of buildings. *AMS 14th Joint Conference on the Applications of Air Pollution Meteorology with the A&WMA*, Atlanta, GA, 2006.
9. Hansen KS, Pedersen KH, Paulsen US. Online wind turbine measurement laboratory. *EWEC*. Athens, Greece, 2006.
10. Vignaroli A. *UniTTe- Nordtank Measurement Campaign (Turbine and Met Masts)*, DTU Wind Energy E. DTU Wind Energy I, 2016. no. 0363.
11. Angelou N, Mann J, Sjöholm M, Courtney M. Direct measurement of the spectral transfer function of a laser based anemometer. *Review of Scientific Instruments* 2012; **83**: 033111.
12. Angelou N, Abari FF, Mann J, Mikkelsen T, Sjöholm M. Challenges in noise removal from doppler spectra acquired by continuous-wave lidar. *Proceedings of the 26th International Laser Radar Conference*, Porto Heli, Greece, 2012.
13. Meyer Forsting AR, Troldborg N. A finite difference approach to despiking in-stationary velocity data - tested on a triple-lidar. *Journal of Physics: Conference Series (Online)* 2016; **753**. DOI: 10.1088/1742-6596/753/7/072017.
14. Angelou N, Sjöholm M. *UniTTe WP3/MC1: Measuring the inflow towards a Nordtank 500 kW turbine using three short-range WindScanners and one SpinnerLidar*, DTU Wind Energy E. DTU Wind Energy, 2015, no. 0093.
15. Mikkelsen TK. *WindScanner.dk - a new Remote Sensing based Research Infrastructure for on- and offshore Wind Energy Research*. National Telford Institute Advanced Research Workshop: Aberdeen, United Kingdom, 2013.
16. Kragh KA, Hansen MH, Mikkelsen T. Precision and shortcomings of yaw error estimation using spinner-based light detection and ranging. *Wind Energy* 2013; **16**: 353–366.
17. Réthoré PE, Sørensen NN. Verification and validation of an actuator disc model. *Wind Energy* 2013; **17**: 919–937.
18. Troen I, Petersen EL. *European Wind Atlas*. Risø National Laboratory: Roskilde, Denmark, 1989.

19. Troldborg N, Zahle F, Réthoré PE, Sørensen NN. Comparison of wind turbine wake properties in non-sheared inflow predicted by different cfd rotor models. *Wind Energy* 2013; **18**: 1239–1250.
20. van der Laan P, Sørensen NN, Réthoré PE, Mann J, Kelly MC, Troldborg N, Schepers JG, Macheffaux E. An improved $k - \epsilon$ model applied to a wind turbine wake in atmospheric turbulence. *Wind Energy* 2014; **18**: 889–907.
21. Sørensen NN. General purpose flow solver applied to flow over hills, *Ph.D. Thesis*, Risø National Laboratory, 1995.
22. Michelsen JA, *Basis3d – a platform for development of multiblock pde solvers. Technical Report*, Technical Report AFM 92-05, Dept. of Fluid Mechanics, Technical University of Denmark, DTU, Lyngby, DK, 1994.
23. Michelsen JA, *Block structured multigrid solution of 2d and 3d elliptic pdes. Technical Report*, Technical Report AFM 94-05, Dept. of Fluid Mechanics, Technical University of Denmark, DTU, Lyngby, DK, 1994.
24. Leonard BP. A stable and accurate convective modelling procedure based on quadratic upstream interpolation. *Computer Methods in Applied Mechanics and Engineering* 1979; **19**: 59–98.
25. Patanker SV, Spalding DB. A calculation procedure for heat, mass and momentum transfer in three-dimensional parabolic flows. *International Journal of Heat and Mass Transfer* 1972.
26. Réthoré PE, Sørensen NN. A discrete force allocation algorithm for modelling wind turbines in computational fluid dynamics. *Wind Energy* 2012; **15**: 915–926.
27. Troldborg N, Sørensen NN, Réthoré PE, van der Laan MP. A consistent method for finite volume discretization of body forces on collocated grids applied to flow through an actuator disk. *Computers & Fluids* 2015; **119**: 197–203.
28. Menter FR. Zonal two equation $k - \omega$ turbulence models for aerodynamic flows. *AIAA Journal* 1993.
29. Meyer Forsting AR, Troldborg N. The effect of blockage on power production for laterally aligned wind turbines. *Journal of Physics: Conference Series (Online)* 2015; **625**: 012029. DOI: 10.1088/1742-6596/625/1/012029.
30. Réthoré PE. Thrust and wake of a wind turbine: relationship and measurements, *Master's Thesis*, Technical University of Denmark, 2007.